Presumido, PH.; Primo Arnau, AM.; Vilar, VJP.; García Gómez, H. (2021). Large area continuous multilayer graphene membrane for water desalination. Chemical Engineering Journal. 413:1-10. https://doi.org/10.1016/j.cej.2020.127510

Large area continuous multilayer graphene membrane for water desalination

Pedro H. Presumido[1], Ana Primo[2], Vítor J.P. Vilar[1*], Hermenegildo Garcia[2*]

[1]*Laboratory of Separation and Reaction Engineering – Laboratory of Catalysis and Materials (LSRE-LCM), Chemical Engineering Department, Faculty of Engineering, University of Porto, Rua Dr. Roberto Frias, 4200-465, Porto, Portugal*

[2]*Instituto de Tecnología Química CSIC-UPV, Universitat Politècnica de València, Consejo Superior de Investigaciones Científicas, Av. de los Naranjos s/n, Valencia, 46022, Spain*

*Corresponding authors:

E-mail addresses: vilar@fe.up.pt (V. Vilar), hgarcia@qim.upv.es (H. Garcia).

Abstract

This manuscript reports the preparation of a large area (84 cm^2) desalination membrane based on multilayers (11 nm thickness) of B,N-codoped defective graphene. The process consists of coating a porous ceramic α-Al_2O_3 support (100 nm pore size) with a continuous nanometric (50 nm) chitosan film containing adsorbed $(NH_4)_3BO_3$. Subsequent pyrolysis in the presence of hydrogen converts chitosan into multilayer defective B,N-codoped graphene. The partial removal of B and N dopant atoms by H_2 during the pyrolysis causes the generation of subnanometric pores due to atom vacancy, as determined by control experiments in the absence of this gas. A NaCl and KCl removal efficiency from brackish water higher than 95 % for a permeate flux of 24.3 L m^{-2} h^{-1} at 10 bars were achieved.

Keywords: Desalination membrane, multilayer graphene membrane, subnanometric pores on graphene, atom vacancies on graphene; dopant removal on graphene.

1. Introduction

Global demand for fresh water has been increasing in recent years [1, 2]. Therefore, technologies aimed at desalination of sea and brackish water are crucial for meeting future demand and improving drinking water quality [3]. In this context, it has been proposed that continuous graphene films can serve to develop the ultimate membranes, since the one-atom thickness represents the physical zero-depth limit for any membrane [4, 5].

Among the many important physical properties of ideal graphene including high electron mobility, optical transparency and remarkable mechanical resistance and elasticity [6], one of relevance for developing membranes is that ideal graphene constitutes a perfect barrier that does not allow the crossover of even the smallest atom or molecule. In particular, it has been proved that a perfect graphene layer cannot permeate He or H_2 at room temperature [7-10] only in exceptional cases where ripples, wrinkles and other defects inducing a local curvature that allow the permeation of H_2 [11]. The major advantages of continuous graphene as membrane that would make its use as a disruptive technology are its high mechanical strength, high elasticity and wide range of chemical stability. Adequate porosity on the graphene sheet should allow to combine a high flux due to the zero depth and high solute removal [12, 13].

The main barriers that limit the general application of desalination technologies to produce fresh water are high pressures required to overcome osmotic pressure and low permeate fluxes, resulting in a high energy consumption. These limitations are closely related to the development of more efficient strong continuous membranes that withstands high pressures and exhibits high salt rejection rate.

In this context, graphene materials have attractive properties for their use in water desalination and purification membranes [14-16]. However, the difficulty to obtain a large area graphene membranes on appropriate supports, together with the lack of suitable strategies to generate pores of proper dimensions to exclude small ions, such as Na^+, K^+ and Cl^-, in a pressurized

filtration process are the two major limitations to be overcome for the wide use of graphene on desalination.

High quality graphene films of sufficiently large area are typically obtained by chemical vapor deposition on metal surfaces, most commonly Ni or Cu. After preparation, it is necessary to devise suitable transfer techniques to deposit this graphene film on the appropriate porous support. Subnanometric porosity has to be, then, subsequently generated by electron or ion impact [17]. Otherwise, porosity on graphene has also been generated by a two-step procedure consisting in O_2 plasma nucleation of defects and subsequent etching and expansion of defects with ozone treatment [18]. The complexity of the process and the need of dedicated equipment reduces the attractiveness and limits the use of graphene as membrane.

To circumvent this limitation, most of the reports so far on the use of graphene and graphene derivatives in desalination membranes are employing this material as additive, rather than as a continuous film, to improve the performance of the embedding polymeric matrix [3, 19]. Alternatively, measurements on graphene membranes have been made on films of micrometric size [14, 20] or larger areas by cumbersome transfer process of costly preformed chemical vapor deposition (CVD) graphene on flat substrates [21, 22]. Besides high-quality graphene [14, 20], other related materials that been also employed for the preparation of desalination membranes include graphene oxide (GO) [23, 24] and boron nitrite (BN) [25-27]. In one of these example, Kim et al. [28] deposited GO nanosheets followed by amino GO nanosheets on the surface of amino polyethersulfone (PES) membrane. The obtained membrane exhibits a good salt rejection of 98 % for a water flux of 28 L m^{-2} h^{-1} at a pressure of 55 bar. In another study, Zahirifar et al. [29] fabricated a membrane through embedment of hexagonal boron nitride (h-BN) in polyvinylidene fluoride (PVDF). The results showed that the best membrane can permeate a flux of 7.1 kg m^{-2} h^{-1} and 99% salt rejection.

Cohen-Tanugi et al. [30] reported theoretical studies based on classical molecular dynamics simulations on the behavior of multilayer graphene membrane for desalination. Their study on models varying the number of overlapped holey graphene layers concluded that a ~200 nm thick nanoporous multilayer graphene membrane should have rejection efficiency and permeate flux similar to those of a single-layer graphene membrane.

There is a clear gap in commercially producing continuous graphene membranes of large area, affordable cost and within quality assurance/quality control requisites [31]. In most of the studies in the field of membranes, graphene is previously prepared by chemical exfoliation of industrial graphite and then is deposited on the support [32-34]. Briefly in this method, graphite is oxidized to graphite oxide that after neutralization is converted to GO. The product is dried to get the GO powder. Lastly, the membrane is immersed in GO solution. However, since graphite particles have, at best, a lateral dimension of a few micrometers, the membrane is constituted by the overlap of micrometric flakes, but it is not a continuous graphene film. Therefore, an innovative method of fabricating large area graphene films that can be used as membranes should be a significant step forward in the area of desalination.

The objective of the present study is to prepare a large area, continuous film of multilayer graphene membrane with subnanometric porosity for water desalination. Preparation procedure and extensive characterization of the multilayer graphene will be correlated with its performance in terms of water flux and salt rejection as a function of applied pressure using brackish water. Due to the excellent rejection rate of NaCl and KCl from brackish water and high permeate flux at lower transmembrane pressure, as well as the large area, the membrane reported herein appears to be easy to implement in water desalination. As far as we know our report describes the largest, continuous graphene membrane with subnanometric pores, where the membrane and the pores have been formed on site in a single step during the preparation process.

2. Experimental section

2.1 Materials

Chitosan (CS) of low molecular weight and boric acid (H_3BO_3) were obtained from Sigma Aldrich (Sigma-Aldrich, St. Louis, MO, USA). Potassium chloride (KCl) and sodium chloride (NaCl) were obtained from Scharlau (Scharlab Chemie, S.A., Barcelona, Spain). Ultrapure water was used in the preparation of all aqueous solutions. KCl and NaCl salts were added in the required amount to reach a final 50 mM concentration. Salt concentration was measured using a calibrated CRISON conductivity meter 524. Microfiltration α-Al_2O_3 membrane (external diameter: 2 cm; internal diameter: 1.6 cm; length: 20 cm; effective membrane area: 84 cm^2) of 100 nm pore size and 40-55% porosity was purchased from Inopor® (Germany).

2.2 Fabrication of continuous multilayer boron, nitrogen-codoped defective graphene film on porous α-Al_2O_3 membrane

Continuous multilayer boron and nitrogen-codoped defective graphene [(B,N)G] films supported on α-Al_2O_3 membrane were prepared similarly to previous report for (B,N)G as powders [35]. Briefly, CS (2.5 g) was dissolved in MilliQ water (250 mL) by addition of 1.7 mL of acetic acid. The viscous gel was filtered under pressure through a Nylon filter (250 µm) to remove insoluble impurities that could be present in the commercial sample. The prepared solution was used to coat the alumina membrane following a dip-coating method with 1 min of contact time. This CS film on alumina membrane was immersed in 250 mL of 25 % aqueous NH_4OH solution containing H_3BO_3 (1.0 g). The CS film impregnated with ammonium borate was pyrolyzed under an argon/hydrogen (5 vol% of H_2) flow (200 mL min^{-1}), increasing the temperature up to 900 °C at a heating rate of 0.9 °C min^{-1}.

2.3 Characterization techniques

Raman spectra were recorded with a Horiba Jobin YvonLabram HR UV–Visible–NIR (200 - 1600 nm) Raman Microscope Spectrometer, using a 632 nm laser as excitation source. AFM

images were recorded with a Veeco apparatus working in tapping mode, using mica as substrate. X-ray photoelectron spectroscopy (XPS) were recorded on a SPECS spectrometer with a Phoibos 150 9 MCD detector using a non-monochromatic X-ray source (Al and Mg) operating at 200 W. For calculation of the binding energies, the peak appearing at 284.4 eV (C1s peak) was used as a reference.

The morphology of the (B,N)G sample, film continuity and thickness were analyzed by scanning electron microscopy (SEM) using a JEOL JSM 6300 apparatus equipped with an X-MAX detector of Oxford Instruments and coupled to a fast ion bombardment (FIB) technique. The crystallinity and structural ordering of the (B,N)G sample were determined by transmission electron microscopy (TEM). TEM images were recorded in a Philips CM300 FEG system with 100 kV operating voltage. TEM samples were obtained by scratching a piece of the membrane with a cutter, suspending it in ethanol by sonication. A microdrop of this suspension was cast onto a carbon-coated copper TEM grid and the solvent evaporated before introducing it into the microscope.

2.4 Permeation test and salt rejection

The experiments were carried out in a membrane reactor (MR). Fig. 1 shows a schematic diagram of the experimental equipment. A thermostated 5 L tank was used to feed the solution into the MR and the temperature maintained at 25°C. The solution was constantly stirred magnetically at 250 rpm. During the experiment, the feed solution was pumped to the MR using a gear pump (Tuthill Pump Group, DGS.68). A laboratory-scale crossflow microfiltration membrane unit was used and the membrane was placed in the middle of the MR. In addition, the system has a pressure controller that was attached to a data collector. The MR worked at a transmembrane pressure of 5, 8 and 10 bar and a crossflow velocity of 10 cm s^{-1}. The whole system was connected by polytetrafluoroethylene (PTFE) tubes.

The permeate was collected in a glass container and the conductivity of the samples was measured to determine salt concentration. Salt concentrations were confirmed by ICP analyses. The permeate flux was estimated by measuring the volume that crosses the membrane in a certain period of time. The maximum pure water flux by the MR (without (B,N)G film coating) was 4.2, 6.8 and 8.5 $m^3\ m^{-2}\ h^{-1}$ for transmembrane pressure of 5, 8 and 10 bar, respectively. After each reaction, the MR unit was washed with ultrapure water and the system flushed for a sufficiently long period of time until the conductivity measurements did not detected the presence of salt in either the feed tank or the membrane permeate. Calculation of the permeate flux and salt rejection efficiency is described in detail in the Supplementary information.

3. Results and discussion

3.1 Large area graphene membrane concept and preparation

The concept of the present desalination membrane has been the preparation of a continuous film of multilayer B and N-codoped defective G on a porous (100 nm) α-Al_2O_3 membrane as support. Rigid ceramic α-Al_2O_3 membrane allows easy handling of the multilayer (B,N)G film and the design of a MR. Notice that the dimensions of the cylindrical membrane is over 80 cm^2 and the procedure can be easily adapted for larger sizes. Thus, the present (B,N)G film corresponds probably to the largest example of a continuous multilayer graphene membrane for desalination ever reported that proves the efficiency of this technology. It should be noted that previous studies have determined graphene performance on micrometric membranes that were 10^{-9} times smaller than the present one [14, 20].

The thermal stability of the ceramic α-Al_2O_3 makes possible the preparation of defective multilayer (B,N)G by pyrolysis of CS containing adsorbed $(NH_4)_3BO_3$. CS is a soluble deacetylated derivative of chitin that is the most important waste from the fishery industry [36]. Previous studies have shown that the pyrolysis of this natural polysaccharide renders a defective N-doped G and that B and N-codoped defective G can be obtained upon pyrolysis of CS

containing $(NH_4)_3BO_3$ [35]. The surface area determined by isothermal N_2 adsorption in powders give values about 80-150 $m^2\ g^{-1}$ with a large micropore size distribution, indicating that as powder the material undergoes extensive stacking due to π–π interactions and van der Waals forces [35]. The success of the continuous multilayer graphene preparation process derives from the ability of CS to form conformal, continuous films on arbitrary substrates and its subsequent transformation into defective doped G upon pyrolysis at 900 ºC [37]. Of note is that during the process of transformation of CS into (B,N)G by thermal treatment at 900 ºC, no detachment or peeling off of the resulting (B,N)G from the alumina tube was observed. The good adherence of graphene film to the Al_2O_3 membrane could reflect a match of the thermal dilatation behavior of both materials and an adequate interaction among the surface of graphene and Al_2O_3. Defects on the resulting G derived from polysaccharides are due to the presence of a residual O content on the final G and the generation of carbon vacancies on the graphene sheet [38]. In addition, the presence of N atoms in a percentage about 5 % has also been established by combustion elemental analysis [39].

The thickness of the resulting defective G layer depends on the thickness of CS precursor. It has been found that during the pyrolysis the thickness of the film decreases by a factor of 5 to 10 fold as consequence of CS dehydration, its structural transformation and packing of the G layers. Although formation of single layers N-doped G has been reported by pyrolysis of very thin CS films on flat substrates [39], the texture of α-Al_2O_3 characterized by a high surface roughness (see SEM images) makes impossible for us the preparation of continuous CS films of the required small thickness. Continuity of the defective G film was considered as a crucial parameter for the preparation of the desalination membrane, since preliminary experiments with these discontinuous defective G films showed that they do not act as barrier for alkali chlorides. For this reason, thicker CS films of 50 nm or larger were necessary to obtain, after pyrolysis, continuous G films. In this regard, it should be commented that the defective nature of the G

films obtained by pyrolysis of CS makes also advisable the stacking of several layers, in a way that the defects and vacancies of one layer that would decrease the selectivity can be masked by the stacking of other layers on top of the defect.

Generation of subnanometric pores to allow water permeation was herein designed by introduction of doping elements on the graphene sheet that subsequently could be removed by suitable chemical treatments. In this regard, it has been found that dopant B atoms on the graphene sheet can be removed either by oxidative treatment and hydrolysis [40] or by thermal hydrogenation [41]. Also dopant N atoms are removed from the graphene sheet by thermal hydrogen treatment [38, 41]. Thus, the hypothesis of the present (B,N)G films as membrane is that by preparing doped or codoped defective multilayer graphene films, subsequent removal of the dopant elements can result, according to DFT modeling of ideal and one-carbon vacancy sheets (see Fig. 2), in the generation of subnanometric pores, able to allow the permeation of H_2O (0.275 nm), but not crossover of hydrated alkali metal ions with hydrated diameters of 0.72 and 0.66 nm for Na^+ and K^+, respectively. As it will be shown below, results of the permeation measurements of brackish water are in accordance with the above hypothesis.

3.2 Characterization of multilayer (B,N)G film supported on porous α-Al_2O_3 membrane

The morphology of the α-Al_2O_3 membrane surface was studied by SEM. Fig. 3 provides two representative images of the fresh and (B,N)G coated α-Al_2O_3 surface. It can be seen there that the fresh α-Al_2O_3 surface is typical of a ceramic material with sintered nanoparticles and significant roughness. The presence of pores in the fresh α-Al_2O_3 membrane is clearly revealed by the images. After forming the (B,N)G membrane, the images show that the whole surface has been completely coated by a conformal film, smoothing the roughness angles and covering the pores. Importantly, SEM images revealed that the film is continuous throughout the whole area.

Fast ion bombardment can dig into the solid surface and makes possible to obtain a cross sectional image of the surface. A representative image is also shown in Fig. 3c. It can be seen there that underneath the thicker layer needed for ion bombardment there is a thin continuous (B,N)G film with a thickness of 11.14 nm (indicated by the green parallel lines). This thin continuous (B,N)G film covers the α-Al_2O_3 membrane characterized by a nanoparticulate morphology and large porosity. Regarding the number of (B,N)G layers corresponding to this thickness, it has been determined that the defective graphene layers pack somewhat loosely than ideal graphene sheets characterized by a short interlayer distance about 0.34 nm. It has been determined by XRD of graphite oxide that graphene oxide layer thickness is around 0.5-0.7 nm and similar values are proposed for defective N-doped graphene [42]. Therefore, the measured thickness of the multilayer (B,N)G film could correspond most probably to between 15 and 20 graphene layers. In the present case, the broadness of the XRD peaks, indicating to a loose packing and low crystallinity, of (B,N)G precludes an estimation of the interlayer distance (see Fig. S1 in Supplementary Information).

High resolution TEM images of the (B,N)G film were taken upon scratching the film from the CS-coated α-Al_2O_3 membrane after pyrolysis (see inset of Fig. 3b for an image of the (B,N)G peeling off), dispersion of the small piece in ethanol by ultrasonication and drop casting onto a TEM sample holder grid. A representative image of the (B,N)G film coating the α-Al_2O_3 membrane is presented also in Fig. 3d. As it can be seen there, the TEM image shows the expected hexagonal structural arrangement characteristic of graphene, in accordance with the previously reported behavior upon pyrolysis of CS at 900 ^oC [39]. In addition, cross-sectional image shows the multilayer stacking of the graphene obtained by pyrolysis, with an inter layer spacing about 0.38 nm corresponding to the expected distance between graphene sheets (see Figure S2 in Supplementary information).

A representative AFM image of the (B,N)G-coated α-Al_2O_3 membrane is presented in Fig. 4. The image shows a frontal view at the micrometric length scale of the (B,N)G film as a smooth surface without the presence of pinholes, cracks or pitches. Additional AFM images showing the surface roughness due to the sintered grains of porous alumina and the continuity of the graphene film are provided in the supporting information. The color codes and panel b of the Fig. 4 refer to differences in height due to the sintering of the coarse grains of micrometric size of Al_2O_3 nanoparticles constituting the substrate on which the (B,N)G film supported. Of note it that while the Al_2O_3 membrane presents apparent holes among the grains corresponding to the submicrometric membrane pores, these discontinuities are coated and not present when the (B,N)G film is on top of the membrane.

Since porous alumina is not a flat surface and in order to better determine the graphene film thickness, the preparation procedure of (B,N)-copoded graphene film was also performed on a flat quartz plate. The corresponding AFM image is presented also in the supporting information. By scratching the graphene film with a cutter and measuring the height profile perpendicular to the scratch, a thickness of 10 nm was also measured for this film, in good agreement with the 11.14 nm thickness determined for the graphene film on porous alumina by fast ion bombardment in SEM measurement.

XPS analysis of the (B,N)G-coated α-Al_2O_3 membrane resulting after pyrolysis at 900 ºC revealed the presence of C, O, N and B elements. Fig. 5a presents the high resolution XPS signals for C1s, O1s, B1s and N1s peaks as well as the best fitting to individual components for each element and their relative atomic proportion. According to XPS analysis over 85 % of the atoms present in (B,N)G correspond to C atoms in three different environments, namely, graphenic, single bonded to N or O and a minor percentage of carboxylate group carbon atoms. The presence of residual O in about 10 at.% from over the 50 % O content of CS precursor was

also recorded, in good agreement with reported data [38]. O atoms double bonded to C (carbonyls) interrupt the graphene lattice and are located at the periphery of the sheet or at holes. Importantly, the presence of about 2 at.% each B and N was also detected, distributed in graphenic dopants and bonded to heteroatoms. In this regard, it has been established that the presence of 5 vol% H_2 in the flow during pyrolysis decreases the percentage of N, respect to samples prepared following the same procedure in Ar flow that contain a N proportion about 5 % [38]. Similarly, it has been found that H_2 at temperatures about 300 ºC removes dopant elements from graphene, this being one reason for doped graphene instability as hydrogenation catalyst [41]. In the case of N-doped defective graphene, evolution of NH_3 was confirmed [41]. These data indicate that the B and N dopant atoms that otherwise become incorporated into the graphene basal plane are partially removed during the pyrolysis by its reaction with H_2 and subsequent evacuation in the effluent gas flushing the system, generating atom vacancies in the graphene sheet. Supplementary information shows optimized DFT models of single and double atom vacancy on the graphene sheet showing the subnanometric pores generated in the process (see Fig. 2 caption). Unfortunately, direct imaging at subnanometric resolution of the atom vacancies by high resolution TEM is not routine due to the lack of graphene stability under high voltage electron beam. In fact, exposure to this high energy electrons has been proposed as a way to generate nanometric pores on graphene sheet [43]. On the other hand, no evidence of larger pores can be obtained by TEM images in the present work or in the precedents that reported the transformation of polysaccharides into graphenes. The importance of doping and H_2 treatment to generate subnanometric pores will be confirmed when commenting the performance as desalination membrane of a control membrane prepared similarly, but in the absence of H_2.

Vibrational spectra of graphenes cannot be obtained by IR spectroscopy, Raman spectra being routine to characterize the nature and type of graphene [35, 39]. Raman spectroscopy of the

(B,N)G-coated α-Al_2O_3 membrane exhibit the expected G and D bands appearing at about 1590 and 1350 cm^{-1} characteristic of defective graphenes, as well as a broad band from 3100 till 2500 cm^{-1}, with maximum about 2700 cm^{-1} corresponding to the 2D peak (Fig. 5b). The broadness of this band is in agreement with the multilayer arrangement of the (B,N)G film, while the relative intensity of the G vs. the D band of 1.2 is coincident to values reported for defective graphenes obtained by pyrolysis of polysaccharides. Overall the Raman spectrum signature confirms the defective graphene nature of the (B,N)G film.

3.3 Performance of (B,N)G films on porous α-Al_2O_3 ceramics as desalination membrane

Preliminary experiments using multilayer N-doped G films on α-Al_2O_3 formed by pyrolysis at 900 ºC under Ar (no H_2) of 50 nm CS films on α-Al_2O_3 ceramic showed no water permeation, indicating that this film behaves as a barrier. In contrast, attempts to obtain thinner CS films on α-Al_2O_3 membranes by coating porous α-Al_2O_3 support with CS aqueous solutions of half the concentration indicated in the experimental section, resulted in membranes without any permeation efficiency, the reason being the lack of continuity of the resulting (B,N)G film. It was also observed that imperfect coating or damage of the coating also result in (B,N)G films without desalination efficiency. Thus, the presence of H_2 in the pyrolysis to partially remove dopant elements and the use of an optimal CS concentration as indicated in the experimental section appear to be conditions necessary to achieve the permeation selectivity described below. Following the preparation procedure indicated in the experimental section, the resulting (B,N)G films were able to achieve selective water transport with high salt rejection. The removal efficiency of NaCl and KCl, permeate flux and pressure effects were determined. The results are summarized in Fig. 6.

One important parameter to be considered in desalination is the pressure dependency of permeate flux and salt rejection since industrial desalinization are operated at very high pressure to achieve sufficiently high flux of purified water [44]. In desalination processes, the external

pressure must be sufficiently greater than the osmotic pressure to make osmosis happen. Usually, the osmotic pressure of seawater is around 23-26 bar with a salt concentration of 32,000 mg L^{-1} [45]. On the other hand, osmotic pressures of brackish water ranges from 1 to 3 bar, for a concentration of 1,000-5,000 mg L^{-1} [45, 46]. Therefore, to achieve osmosis, feed pressures applied to brackish water may vary from 5 [47] to 55 bar [28]. In the present study, to prove the selectivity in salt removal, a concentration in the typical range of brackish waters of 50 mM was selected. This concentration value corresponds to 2,925 and 3,725 mg L^{-1} for NaCl and KCl, respectively.

As the pressure in the MR increases, the permeate flow in the (B,N)G-coated α-Al_2O_3 membrane increased as expected according to Darcy's law. The permeation values for (B,N)G-coated α-Al_2O_3 membrane were from 12.3 and 7.6 L m^{-2} h^{-1} (5 bar) to 24.3 and 15.1 L m^{-2} h^{-1} (10 bar) for KCl and NaCl, respectively. In this range of pressure (5 to 10 bars) the water flux varies linearly with the pressure. However, this linearity between water flux and pressure could not apply to higher pressures, since these conditions could decrease membrane permeation due to compaction and morphological changes.

The influence from increasing from 8 bar to 10 bar on the permeation flow was not significant with an increase of 2.1 and 5.2 % for KCl and NaCl, respectively. This can be explained by assuming that once the external pressure exerted on the reactor is sufficiently high to overcome the osmotic pressure, the limiting factor is pore density on the membrane that allows the permeation to happen, approaching a plateau for the water flux with the pressure.

As it can be seen in Fig. 6, there is a remarkable difference in the water flux as a function of the nature of the alkali metal chloride salt. The maximum difference in the water flux for the two salts can be as high as 66 % larger for KCl respect to NaCl for the 10 bar pressure measurement, a fact that is remarkable. The difference in water flux is proposed to be related to the difference in size of K^+ and Na^+ ions that should be close to the effective pore size of the (B,N)G

membrane. In principle, K^+ has a larger ionic radius (1.32 Å) than Na^+ (0.93 Å), because it has a larger number of atomic orbital shells and electrons surrounding the nucleus. However, for hydrated ions, Na^+ is a larger ion, since its higher polarization effect determines a stronger attractive force on neighboring water molecules. As a consequence, Na^+ (3.60 Å) has a larger hydration radius than K^+ (3.30 Å) [48]. Since the radius of hydrated ions are significantly larger than the radius of isolated water molecules passing through the membrane, a selectivity should be expected for pores of adequate dimensions as those predicted by the models in Fig. 2. The pore sizes of the membrane are very important and critical in this case. Cohen-Tanugi et al. [30] found that a graphene membrane with radius of 0.3 nm exhibited full salt rejection. Others authors show that most salt ions can pass through pores of a diameter above 0.55 nm [18]. Thus, the available experimental data indicates that in the case of (B,N)G films the pore radius should be around 0.3 nm, in addition to the presence of residual percentage of B, N and O heteroatoms. Under these circumstances, interaction of hydrated Na^+ with the pore rims can result in partial dynamic clogging of the pores and, therefore, lower fluxes should be observed for Na^+, since the larger radius of K^+ makes this interaction with the pore entrances much weaker. Thus, the different behavior of NaCl and KCl constitutes an indirect evidence of the effective pore diameter that should be in a narrow window close to the Na^+ ions able to discriminate in such a notable percentage between Na^+ and K^+ sizes.

As it can be seen also in Fig. 6, (B,N)G membrane exhibited high salt rejection efficiency value for both NaCl and KCl around 98.0 and 98.5 % for pressures of 5, 8 and 10 bar. Commercial desalination membranes generally exhibit more than 98 % NaCl rejection, but there is a relationship between water flow and salt rejection, as GO membranes with higher rejection efficiency must operate at relatively low water flux [14]. Other studies also had high salt rejection rates around 98-99 %, but with higher pressures or with permeate flow smaller than the current study [49]. Thus, the (B,N)G-coated α-Al_2O_3 membrane reported here outperforms

commercial and most of the previous reported graphene desalination membranes by achieving high water flux and high salt rejection rate at pressures of 8 bars for 50 mM salt concentration. To put the results shown in Fig. 6 into context, Table 1 summarizes the performance data from other studies based on the use of graphene and graphene oxide in combination or not with a support. The performance of (B,N)G-coated α-Al_2O_3 membrane showed relatively good performance in terms of water flow as well as excellent salt rejection compared to other filtration membranes. It should be, however, stressed that the previous report on the performance of single layer graphene refers to a measurement on a membrane of 5 μm diameter that is about 1 billion times smaller area than the one under study here.

Another factor that directly affects the permeate flux is salt concentration. In general, the water permeate flux decreases as the solute concentration increased. The same effect is also observed here for (B,N)G-coated α-Al_2O_3 membrane with a flux for 12 and 50 mM NaCl solutions of 36.4 and 7.6 L m^{-2} h^{-1}, respectively, at 5 bar pressure; the corresponding values for salt rejection were 95.7 and 98.5%, respectively (Fig. 6b). A change of feed concentration directly affects sorption at the liquid/membrane interface. Therefore, hydrated ion concentration on the membrane near or at the pores increases with feed solution concentration, causing a decrease in the water flow [50]. Observation of the strong influence of NaCl concentration on the permeate flux is again in agreement with the previous justification of the different permeate flux between NaCl and KCl based on the assumption that the effective pore radius size of (B,N)G film should be close to the hydrated radius of the Na^+ ion, about 0.36 nm.

Regarding the filtration mechanism, it is important to rule out that selectivity of the salt retention is not due to adsorption of the salt on the graphene. Considering the theoretical graphene density of 2.26 g cm^{-3}, the area (84 cm^2) and the average thickness (11 nm), the graphene mass in the membrane is estimated as 0.2 mg, while the total amount of NaCl flushed through the membrane in 5 h at 10 bar is 18.90 mol, corresponding to 1098.8 g. To further

determine the adsorption capacity of (B,N)G for NaCl, 50 mg of (B,N)G (about 250 times higher amount than the amount of (B,N)G on the alumina membrane) was added to 25 mL of a 50 mM aqueous solution of NaCl (same concentration as in the permeation measurements), observing a negligible decrease in NaCl concentration. Figure S3 in supporting information provides the temporal profile of the isothermal NaCl adsorption.

4. Conclusions

The present study reports a new concept for the preparation of large area desalination membranes based *on site* formation of multilayer defective graphene with subnanometric pores. The process derives from the ability of chitosan to form conformal nanometric films that can be subsequently transformed into multilayer doped defective graphene. The pyrolysis conditions can be adapted to form atom vacancies on the graphene sample. Considering that chitosan is a low value waste material, that the procedure based on dip coating and pyrolysis can serve to prepare large area membranes at low cost and without requiring dedicated CVD systems. The (B,N)G membrane exhibits a remarkable permeation selectivity. Thus, the present report may constitute a significant advance in desalination technology providing suitable preparation procedure and low cost desalination membrane not only on flat, but also in curved supports. It can also be anticipated that the procedure can be easily adapted to obtain analogous membranes based on defective graphene with controlled pore sizes for different applications.

Acknowledgments

This work was financially supported by: i) Project NOR-WATER funded by INTERREG VA Spain-Portugal cooperation programme, Cross-Border North Portugal/Galiza Spain Cooperation Program (POCTEP) and ii) Project POCI-01-0145-FEDER-006984 – Associate Laboratory LSRE-LCM funded by FEDER funds through COMPETE2020 - Programa Operacional Competitividade e Internacionalização (POCI) – and by national funds through FCT - Fundação para a Ciência e a Tecnologia. P.H. Presumido acknowledges FCT for his scholarship (SFRH/BD/138756/2018). V.J.P. Vilar acknowledges the FCT Individual Call to Scientific Employment Stimulus 2017 (CEECIND/01317/2017). Financial support by the Spanish Ministry of Science and Innovation (Severo Ochoa SEV2016 and RTI2018-890237-CO_2-R1) and Generalitat Valenciana (Prometeo 2017-83) is also gratefully acknowledged.

References

[1] P.H. Gleick, Global freshwater resources: soft-path solutions for the 21st century, Science 302 (2003) 1524-1528.
[2] P.H. Gleick, The human right to water, Water Policy 1 (1998) 487-503.
[3] J.R. Werber, C.O. Osuji, M. Elimelech, Materials for next-generation desalination and water purification membranes, Nat. Rev. Mater. 1 (2016) 1-15.
[4] K. Celebi, J. Buchheim, R.M. Wyss, A. Droudian, P. Gasser, I. Shorubalko, J.-I. Kye, C. Lee, H.G. Park, Ultimate Permeation Across Atomically Thin Porous Graphene, Science 344 (2014) 289-292.
[5] G. He, S. Huang, L.F. Villalobos, J. Zhao, M. Mensi, E. Oveisi, M. Rezaei, K.V. Agrawal, High-permeance polymer-functionalized single-layer graphene membranes that surpass the postcombustion carbon capture target, Energy & Environmental Science 12 (2019) 3305-3312.
[6] A.K. Geim, K.S. Novoselov, The rise of graphene, Nat. Mater. 6 (2007) 183–191.
[7] J.S. Bunch, S.S. Verbridge, J.S. Alden, A.M. Van Der Zande, J.M. Parpia, H.G. Craighead, P.L. McEuen, Impermeable atomic membranes from graphene sheets, Nano Lett. 8 (2008) 2458-2462.
[8] F. Guo, G. Silverberg, S. Bowers, S.-P. Kim, D. Datta, V. Shenoy, R.H. Hurt, Graphene-based environmental barriers, Environ. Sci. Technol. 46 (2012) 7717-7724.
[9] M.-S. Cao, X.-X. Wang, W.-Q. Cao, J. Yuan, Ultrathin graphene: electrical properties and highly efficient electromagnetic interference shielding, J. Mater. Chem. C 3 (2015) 6589-6599.
[10] V. Berry, Impermeability of graphene and its applications, Carbon 62 (2013) 1-10.
[11] P.Z. Sun, Q. Yang, W.J. Kuang, Y.V. Stebunov, W.Q. Xiong, J. Yu, R.R. Nair, M.I. Katsnelson, S.J. Yuan, I.V. Grigorieva, M. Lozada-Hidalgo, F.C. Wang, A.K. Geim, Limits on gas impermeability of graphene, Nature 579 (2020) 229-232.
[12] X. Wang, X. Ba, N. Cui, Z. Ma, L. Wang, Z. Wang, X. Gao, Preparation, characterisation, and desalination performance study of cellulose acetate membranes with MIL-53(Fe) additive, J. Membrane Sci. 590 (2019) 1-9.
[13] K.A. Mahmoud, B. Mansoor, A. Mansour, M. Khraisheh, Functional graphene nanosheets: The next generation membranes for water desalination, Desalination 356 (2015) 208-225.
[14] S.P. Surwade, S.N. Smirnov, I.V. Vlassiouk, R.R. Unocic, G.M. Veith, S. Dai, S.M. Mahurin, Water desalination using nanoporous single-layer graphene, Nat. Nanotechnol. 10 (2015) 459-464.
[15] D. Cohen-Tanugi, J.C. Grossman, Mechanical strength of nanoporous graphene as a desalination membrane, Nano Lett. 14 (2014) 6171-6178.
[16] E.N. Wang, R. Karnik, Water desalination: Graphene cleans up water, Nat. Nanotechnol. 7 (2012) 552-554.
[17] H.W. Yoon, Y.H. Cho, H.B. Park, Graphene-based membranes: status and prospects, Philos. T. Roy. Soc. A 374 (2016) 1-23.
[18] J. Zhao, G. He, S. Huang, L.F. Villalobos, M. Dakhchoune, H. Bassas, K.V. Agrawal, Etching gas-sieving nanopores in single-layer graphene with an angstrom precision for high-performance gas mixture separation, Science Advances 5 (2019) eaav1851.
[19] M.E. Ali, L. Wang, X. Wang, X. Feng, Thin film composite membranes embedded with graphene oxide for water desalination, Desalination 386 (2016) 67-76.
[20] S.C. O'Hern, M.S.H. Boutilier, J.-C. Idrobo, Y. Song, J. Kong, T. Laoui, M. Atieh, R. Karnik, Selective Ionic Transport through Tunable Subnanometer Pores in Single-Layer Graphene Membranes, Nano Lett. 14 (2014) 1234-1241.

[21] P.R. Kidambi, D. Jang, J.-C. Idrobo, M.S.H. Boutilier, L. Wang, J. Kong, R. Karnik, Nanoporous Atomically Thin Graphene Membranes for Desalting and Dialysis Applications, Advanced Materials 29 (2017) 1700277.
[22] F.M. Kafiah, Z. Khan, A. Ibrahim, R. Karnik, M. Atieh, T. Laoui, Monolayer graphene transfer onto polypropylene and polyvinylidenedifluoride microfiltration membranes for water desalination, Desalination 388 (2016) 29-37.
[23] J. Abraham, K.S. Vasu, C.D. Williams, K. Gopinadhan, Y. Su, C.T. Cherian, J. Dix, E. Prestat, S.J. Haigh, I.V. Grigorieva, P. Carbone, A.K. Geim, R.R. Nair, Tunable sieving of ions using graphene oxide membranes, Nat. Nanotechnol. 12 (2017) 1-6.
[24] R. Mukherjee, P. Bhunia, S. De, Nanofiltration range desalination by high flux graphene oxide impregnated ultrafiltration hollow fiber mixed matrix membrane, J. Clean. Prod. 213 (2019) 393-405.
[25] J. Azamat, A. Khataee, Molecular dynamics simulations of removal of cyanide from aqueous solution using boron nitride nanotubes, Comp. Mater. Sci. 128 (2017) 8-14.
[26] J. Azamat, A. Khataee, Removal of nitrate ion from water using boron nitride nanotubes: Insights from molecular dynamics simulations, Comput. Theor. Chem. 1098 (2016) 56-62.
[27] L. Zhang, L. Jia, J. Zhang, J. Li, L. Liang, Z. Kong, J.-W. Shen, X. Wang, W. Zhang, H. Wang, Understanding the effect of chemical modification on water desalination in boron nitride nanotubes via molecular dynamics simulation, Desalination 464 (2019) 84-93.
[28] S.G. Kim, D.H. Hyeon, J.H. Chun, B.-H. Chun, S.H. Kim, Novel thin nanocomposite RO membranes for chlorine resistance, Desalination and Water Treatment 51 (2013) 6338-6345.
[29] J. Zahirifar, A. Hadi, J. Karimi-Sabet, A. Dastbaz, Influence of hexagonal boron nitride nanosheets as the additives on the characteristics and performance of PVDF for air gap membrane distillation, Desalination 460 (2019) 81-91.
[30] D. Cohen-Tanugi, L.-C. Lin, J.C. Grossman, Multilayer Nanoporous Graphene Membranes for Water Desalination, Nano Lett. 16 (2016) 1027-1033.
[31] A. Boretti, S. Al-Zubaidy, M. Vaclavikova, M. Al-Abri, S. Castelletto, S. Mikhalovsky, Outlook for graphene-based desalination membranes, npj Clean Water 1 (2018) 1-11.
[32] H.-H. Huang, R.K. Joshi, K.K.H. De Silva, R. Badam, M. Yoshimura, Fabrication of reduced graphene oxide membranes for water desalination, J. Membrane Sci. 572 (2019) 12-19.
[33] M. Safarpour, A. Khataee, V. Vatanpour, Thin film nanocomposite reverse osmosis membrane modified by reduced graphene oxide/TiO2 with improved desalination performance, J. Membrane Sci. 489 (2015) 43-54.
[34] H. Khorramdel, E. Dabiri, F.F. Tabrizi, M. Galehdari, Synthesis and characterization of graphene acid membrane with ultrafast and selective water transport channels, Sep. Purif. Technol. 212 (2019) 497-504.
[35] A. Dhakshinamoorthy, A. Primo, P. Concepcion, M. Alvaro, H. Garcia, Doped graphene as a metal-free carbocatalyst for the selective aerobic oxidation of benzylic hydrocarbons, cyclooctane and styrene, Chem.-Eur. J. 19 (2013) 7547-7554.
[36] D. Elieh-Ali-Komi, M.R. Hamblin, Chitin and chitosan: production and application of versatile biomedical nanomaterials, Int. J. Adv. Res. 4 (2016) 411-427.
[37] J. Niu, A. Domenech-Carbó, A. Primo, H. Garcia, Uniform nanoporous graphene sponge from natural polysaccharides as a metal-free electrocatalyst for hydrogen generation, RSC Adv. 9 (2019) 99-106.
[38] J. He, A. Anouar, A. Primo, H. García, Quality Improvement of Few-Layers Defective Graphene from Biomass and Application for H2 Generation, Nanomaterials 9 (2019) 1-15.
[39] A. Primo, P. Atienzar, E. Sanchez, J.M. Delgado, H. García, From biomass wastes to large-area, high-quality, N-doped graphene: catalyst-free carbonization of chitosan coatings on arbitrary substrates, Chemical Communications 48 (2012) 9254-9256.

[40] J.C. Espinosa, S. Navalón, A. Primo, M. Moral, J.F. Sanz, M. Álvaro, H. García, Graphenes as Efficient Metal-Free Fenton Catalysts, Chem.-Eur. J. 21 (2015) 11966-11971.
[41] A. Primo, F. Neatu, M. Florea, V. Parvulescu, H. Garcia, Graphenes in the absence of metals as carbocatalysts for selective acetylene hydrogenation and alkene hydrogenation, Nat. Commun. 5 (2014) 1-9.
[42] S. Ray, Applications of graphene and graphene-oxide based nanomaterials, William Andrew2015.
[43] H.W. Yoon, Y.H. Cho, H.B. Park, Graphene-based membranes: status and prospects, Philosophical Transactions of the Royal Society A: Mathematical, Physical and Engineering Sciences 374 (2016) 20150024.
[44] K.P. Lee, T.C. Arnot, D. Mattia, A review of reverse osmosis membrane materials for desalination—Development to date and future potential, J. Membrane Sci. 370 (2011) 1-22.
[45] A. Sagle, B. Freeman, Fundamentals of Membranes for Water Treatment in: J.A. Arroyo (Ed.) The Future of Desalination in Texas, Texas Water Development Board, Austin, TX, 2004.
[46] C. Fritzmann, J. Löwenberg, T. Wintgens, T. Melin, State-of-the-art of reverse osmosis desalination, Desalination 216 (2007) 1-76.
[47] S. Kim, R. Ou, Y. Hu, X. Li, H. Zhang, G.P. Simon, H. Wang, Non-swelling graphene oxide-polymer nanocomposite membrane for reverse osmosis desalination, J. Membrane Sci. 562 (2018) 47-55.
[48] L.B. Railsback, Some Fundamentals of Mineralogy and Geochemistry, Department of Geology, University of Georgia, Athens, Georgia, 2006.
[49] M. Akhavan, J. Schofield, S. Jalili, Water transport and desalination through double-layer graphyne membranes, Phys. Chem. Chem. Phys. 20 (2018) 13607-13615.
[50] B. Liang, W. Zhan, G. Qi, S. Lin, Q. Nan, Y. Liu, B. Cao, K. Pan, High performance graphene oxide/polyacrylonitrile composite pervaporation membranes for desalination applications, J. Mater. Chem. A 3 (2015) 5140-5147.
[51] D.H. Seo, S. Pineda, Y.C. Woo, M. Xie, A.T. Murdock, E.Y.M. Ang, Y. Jiao, M.J. Park, S.I. Lim, M. Lawn, F.F. Borghi, Z.J. Han, S. Gray, G. Millar, A. Du, H.K. Shon, T.Y. Ng, K. Ostrikov, Anti-fouling graphene-based membranes for effective water desalination, Nature Communications 9 (2018) 683.
[52] J. Yin, G. Zhu, B. Deng, Graphene oxide (GO) enhanced polyamide (PA) thin-film nanocomposite (TFN) membrane for water purification, Desalination 379 (2016) 93-101.
[53] M. Safarpour, A. Khataee, V. Vatanpour, Thin film nanocomposite reverse osmosis membrane modified by reduced graphene oxide/TiO2 with improved desalination performance, Journal of Membrane Science 489 (2015) 43-54.
[54] B.M. Ganesh, A.M. Isloor, A.F. Ismail, Enhanced hydrophilicity and salt rejection study of graphene oxide-polysulfone mixed matrix membrane, Desalination 313 (2013) 199-207.

Figures Captions

Fig. 1. The schematic diagram of the laboratory-scale crossflow microfiltration membrane unit. Note: TM - thermometer, (B,N)G - multilayer (B,N)G membrane (for preparation procedure of the (B,N)G membrane on porous alumina see section 2.2).

Fig. 2. Model of an ideal graphene sheet (left) and a model graphene sheet having one or two atom carbon vacancies (right). The concept of the present (B,N)G film as desalination membrane is based on the atomic radius distances among the carbon atoms around vacancies that are about 0.36 nm, in the range wanted for selective H_2O permeation. Note that besides C atoms, defective (B,N)G film contains B, N and O heteroatoms.

Fig. 3. SEM image of membrane surface (a) without and (b) with (B,N)G film; (c) FIB image to measure (B,N)G film thickness indicated by green parallel lines underneath the thick layer needed for taking the image; high resolution TEM of (d) (B,N)G film. The inset of panel b shows a small debris scratched from the graphene membrane to perform the high resolution TEM images of the (B,N)G film shown in panel d.

Fig. 4. Frontal wide-field AFM image of (B,N)G-coated α-Al_2O_3 membrane with the height scale color codes (upper frame) and the height variation along the red and blue lines marked in frontal view (bottom frame). This image shows the continuity of the (B,N)G films and the absence of cracks and pinholes on it.

Fig. 5. (a) High resolution XP spectra of C1s, O1s, B1s and N1s peaks, together with the best fitting to individual components, indicating their corresponding binding energy values, atomic proportion and assignment. (b) Raman spectra of (B,N)G film on α-Al_2O_3 membrane upon 632 nm excitation and the assignment of the vibrational bands.

Fig. 6. (a) Effects of transmembrane pressure on (B,N)G-coated α-Al_2O_3 membrane water flow for NaCl (●) and KCl (■) salts as well as the rejection percentage of NaCl (○) and KCl (□)

([NaCl]=[KCl] = 50 mM); (b) Effects of feed NaCl concentration on the desalination performance of the (B,N)G-coated α-Al_2O_3 membrane (Pressure = 5 bar).

Fig. 1

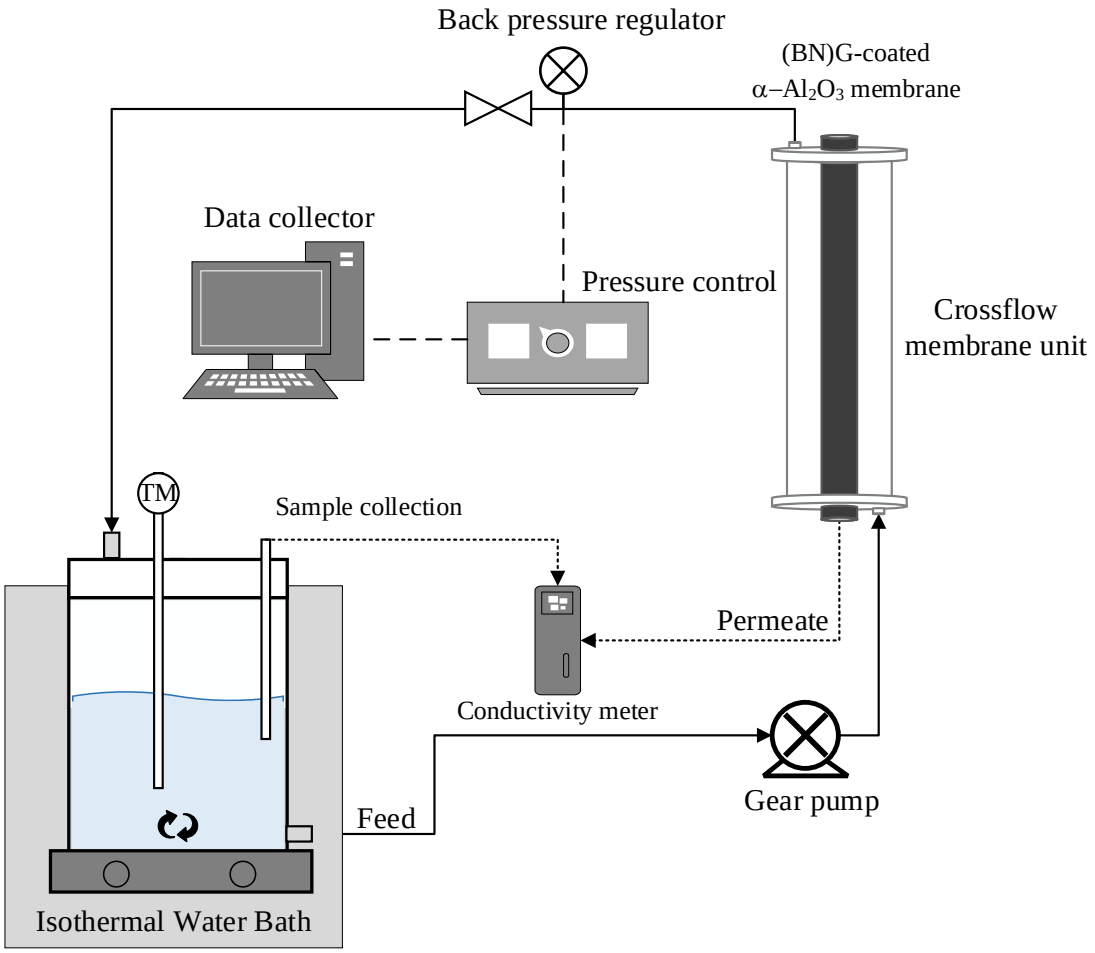
Back pressure regulator
(BN)G-coated
α–Al2O3 membrane
Data collector
Pressure control
Crossflow
membrane unit
TM
Sample collection
Permeate
Conductivity meter
Gear pump
Feed
Isothermal Water Bath

Fig. 2

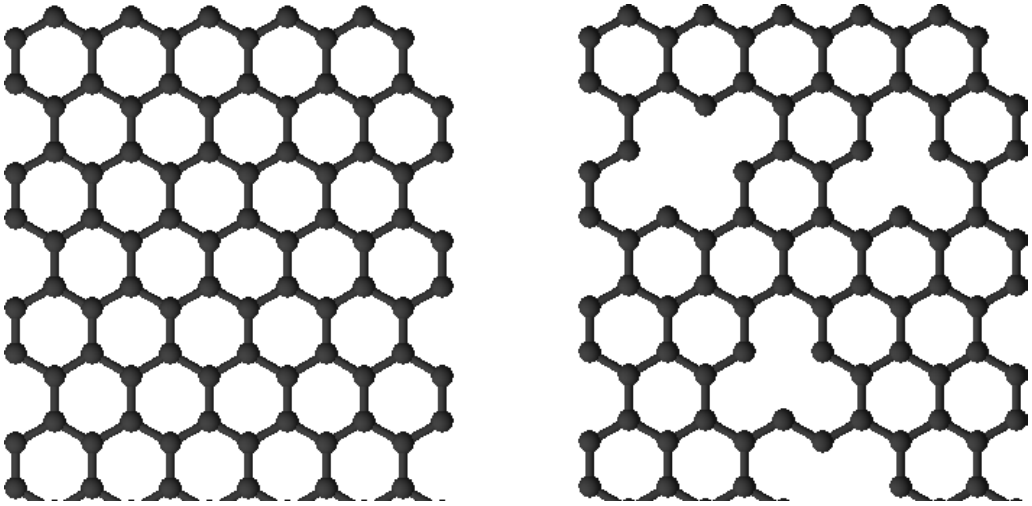

Fig. 3

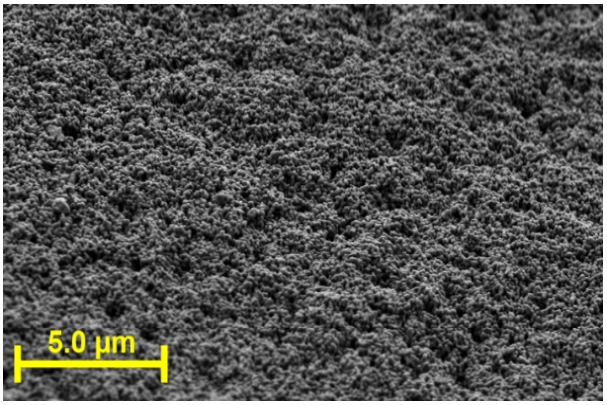

(a)

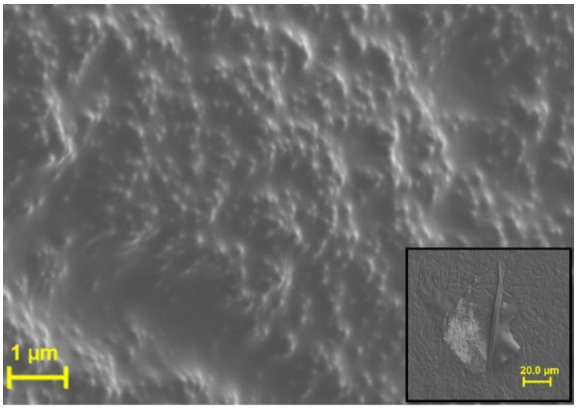

(b)

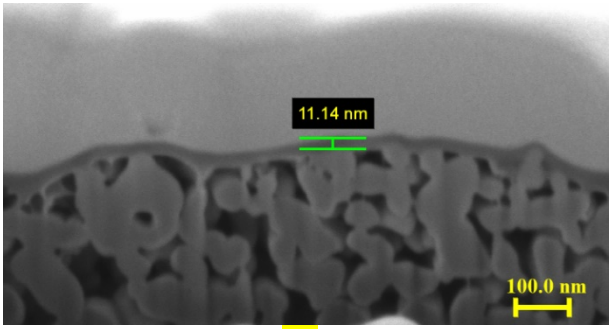

(c)

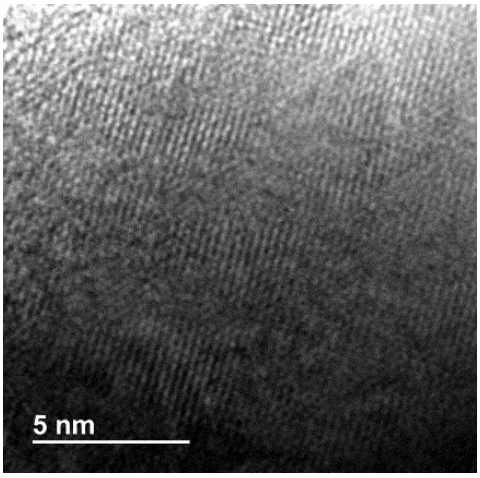

(d)

Fig. 4

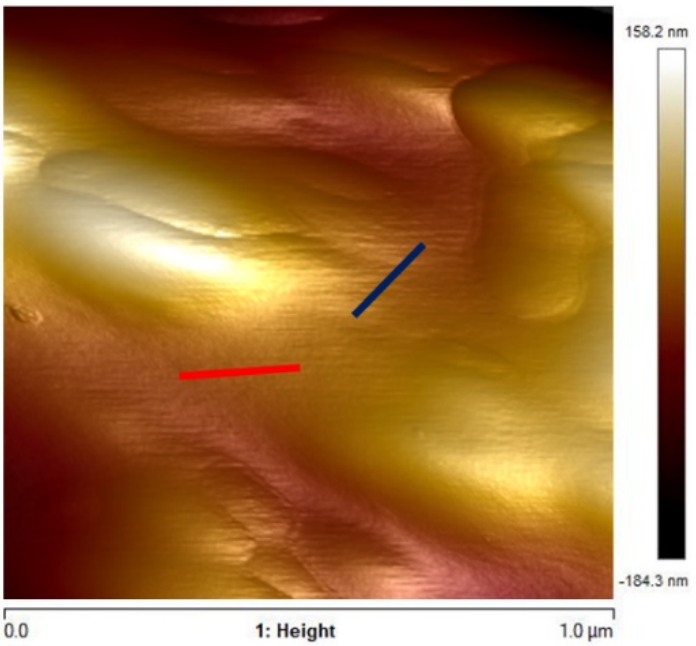
158.2 nm
-184.3 nm
0.0
1: Height
1.0 µm

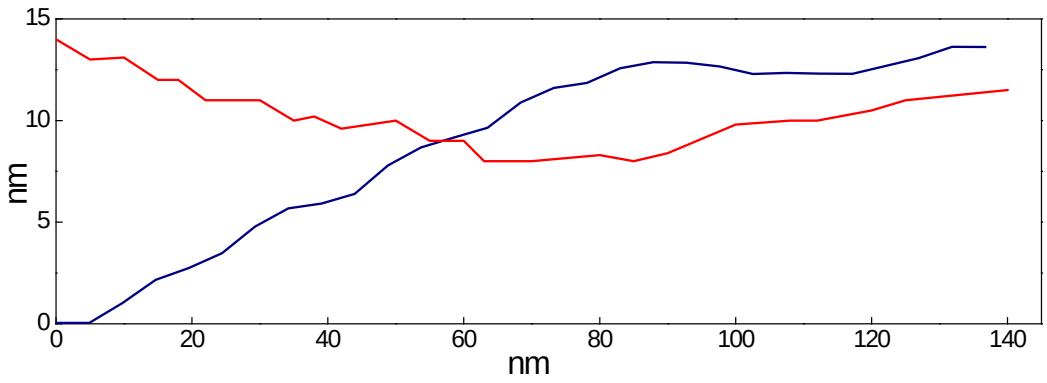
15
10
5
0
nm
0
20
40
60
80
100
120
140
nm

Fig. 5

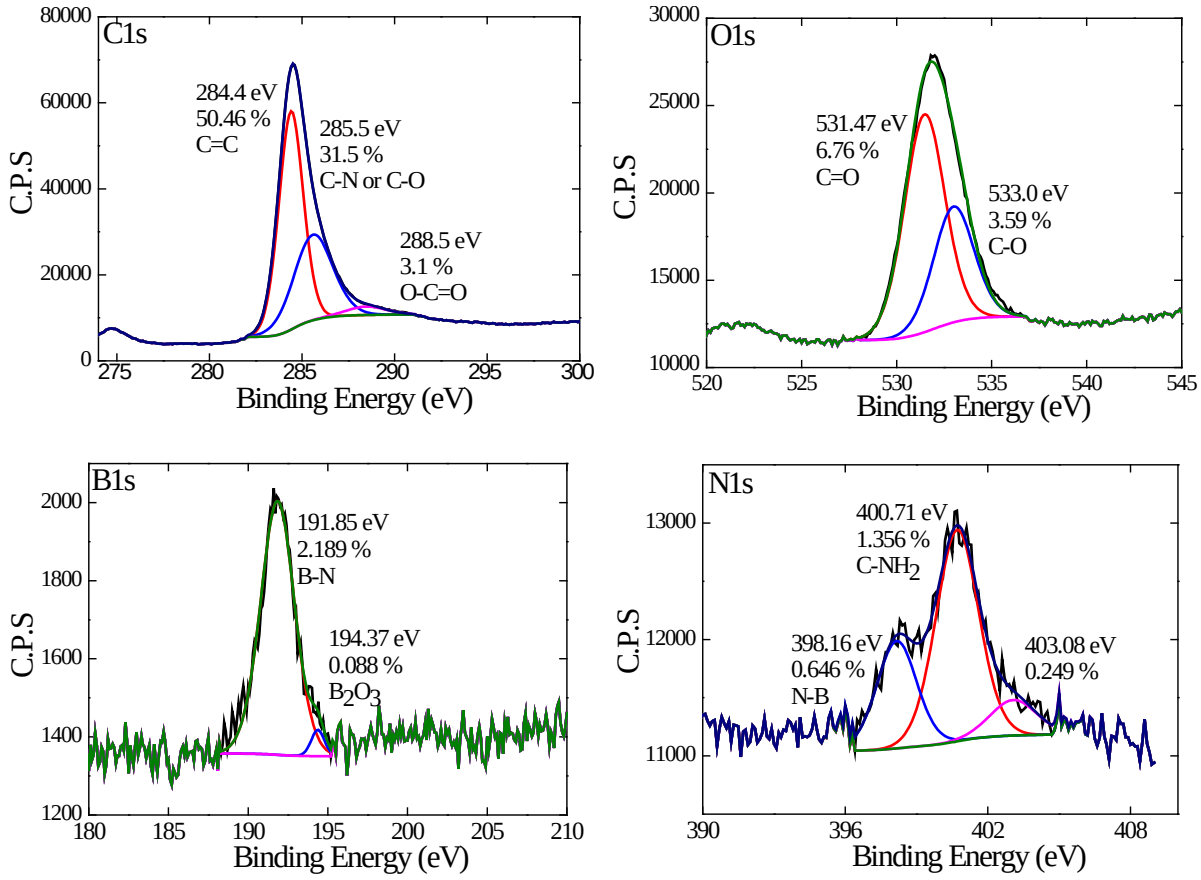
C1s
284.4 eV
50.46 %
C=C
285.5 eV
31.5 %
C-N or C-O
288.5 eV
3.1 %
O-C=O
C.P.S
Binding Energy (eV)
O1s
531.47 eV
6.76 %
C=O
533.0 eV
3.59 %
C-O
C.P.S
Binding Energy (eV)
B1s
191.85 eV
2.189 %
B-N
194.37 eV
0.088 %
B2O3
C.P.S
Binding Energy (eV)
N1s
400.71 eV
1.356 %
C-NH2
398.16 eV
0.646 %
N-B
403.08 eV
0.249 %
C.P.S
Binding Energy (eV)

(a)

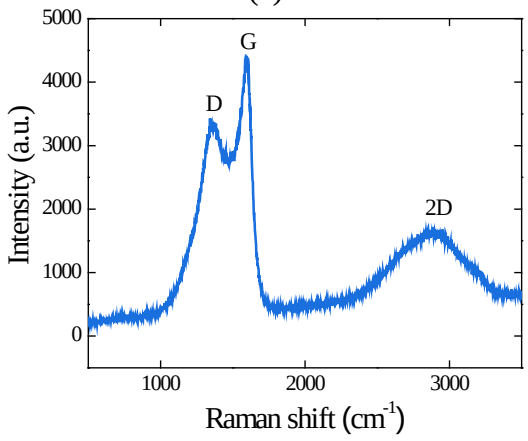
G
D
2D
Intensity (a.u.)
Raman shift (cm-1)

(b)

Fig. 6

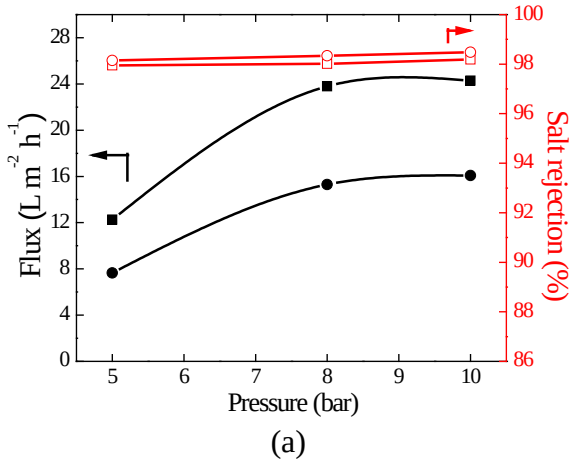
Flux (L m-2 h-1)
Salt rejection (%)
Pressure (bar)
0
4
8
12
16
20
24
28
86
88
90
92
94
96
98
100
5
6
7
8
9
10

(a)

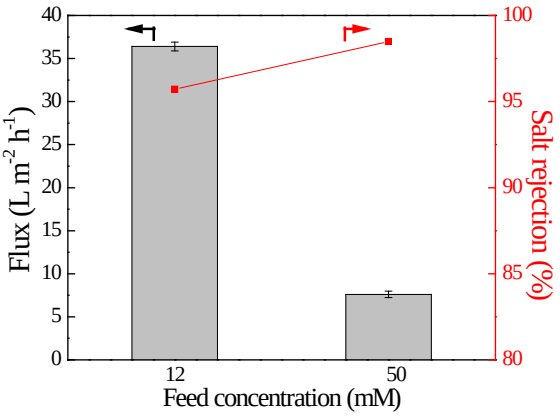
Flux (L m-2 h-1)
Salt rejection (%)
Feed concentration (mM)
0
5
10
15
20
25
30
35
40
80
85
90
95
100
12
50

(b)

Table 1. Overview of reported data on graphene-based water desalination membranes and relevant operation conditions.

Membrane material	**Preparation method**	**Membrane area (cm^2)**	**Feed concentration**	**Flux ($L \cdot m^{-2} \cdot h^{-1}$)**	**Pressure (bar)**	**Rejection (%)**	**Ref.**
GO-PAN	Hummers method and vacuum filtration of GO particles	14.7	35000 ppm	14.3 - 65.1	10	99.8	[50]
GO-PTFE	CVD graphene on flat substrates and poly (methyl methacrylate) (PMMA)-assisted transfer of graphene was adopted	4	70000 ppm	50	-	99.9	[51]
GO-PA	Hummers method and coating method	9.6	2000 ppm	59.4	20	94	[52]
GO-PS	Brodie method and layer-by-layer method	12.56	300 ppm	28	55	98	[28]
rGO/TiO_2-PSf	Hummers method and phase inversion method	36	2000 ppm	51.3	15	99.45	[53]
GO-PES	Hummers method and the precursor solution was filtered through the membrane	14.6	2000 ppm	35.6	10	98.5	[47]
GO-PSf	Brodie's method and phase inversion method	19.6	1000 ppm	10	4	40-60	[54]
GO-PVDF	Hummers method and pressure assisted self-assembly	4.8	2000 ppm	73.2	15	95.6	[34]
(B,N)G	CS film impregnated in the membrane with ammonium borate was pyrolyzed.	84	50 mM (± 3725 ppm)	24.3	10	98.5	This work

Note: GO – graphene oxide; PAN – Polyacrylonitrile; PTFE – polytetrafluoroethylene; PA – Polyamide; PS – polysulfone; PSf – Polysulfone; PES - Poly(ether sulfones); PVDF – Polyvinylidene fluoride; CVD – Chemical vapour deposition; (B,N)G – graphene-boron nitride.